

Demixing fluorescence time traces transmitted by multimode fibers

Caio Vaz Rimoli^{1,2}, Claudio Moretti¹, Fernando Soldevila¹, Enora Brémont²,
Cathie Ventalon^{2*}, Sylvain Gigan^{1*}

¹Laboratoire Kastler Brossel, ENS-Universite PSL, CNRS, Sorbonne Universite, College de France, 24 Rue Lhomond, Paris, F-75005, France.

²IBENS, Departement de Biologie, Ecole Normale Superieure, CNRS, Inserm, PSL Research University, 46 Rue d'Ulm, Paris, F-75005, France.

*Corresponding author(s). E-mail(s): cathie.ventalon@bio.ens.psl.eu; sylvain.gigan@lkb.ens.fr.

Contributing authors: caio.vaz-rimoli@lkb.ens.fr; claudio.moretti@lkb.ens.fr;

fernando.soldevila@lkb.ens.fr; enora.bremont@edu.bio.ens.psl.eu

Abstract

Fiber photometry is a significantly less invasive method compared to other deep brain imaging microendoscopy approaches due to the use of thin multimode fibers (MMF diameter < 500 μm). Nevertheless, the transmitted signals get scrambled upon propagation within the MMF, thus limiting the technique's potential in resolving temporal readouts with cellular resolution. Here, we demonstrate how to separate the time trace signals of several fluorescent sources probed by a thin ($\approx 200 \mu\text{m}$) MMF with typical implantable length in a mouse brain. We disentangled several spatio-temporal fluorescence signals by using a general unconstrained non-negative matrix factorization (NMF) algorithm directly on the raw video data. Furthermore, we show that commercial and low-cost open-source miniscopes display enough sensitivity to image the same fluorescence patterns seen in our proof of principle experiment, suggesting that a whole new avenue for novel minimally invasive deep brain studies with multimode fibers in freely-behaving mice is possible.

Keywords: Spatio-temporal demixing, time traces, scattering fingerprints, transient patterns, short multimode fiber, neuronal microendoscopy, non-negative matrix factorization.

1. Introduction

Fluorescence-based techniques are providing researchers with different ways to collect functional readouts from neuronal activity in the brain^{1–10}. However, measuring neuronal activity at depths greater than 1 mm is still challenging mainly due to issues resulting from light scattering, especially in prominent paradigms such as freely behaving animals^{11–14}. To address this problem, neuronal microendoscopy methods have emerged as complementary alternatives to linear and nonlinear fluorescence microscopy techniques for studying neuronal activity in deep brain regions using genetically encoded calcium indicators (GECI)^{13–16}. Among these methods, conventional microendoscopic methods that use a single gradient index (GRIN) lens optics^{16–19}, as well as fiber photometry recordings using multimode fiber (MMF)^{15,20–23}, have been successfully used to obtain functional neuronal activity signals in deep brain regions in freely behaving mice^{15,22,24}. Nonetheless, direct imaging techniques and fiber photometry approaches bring peculiar tradeoffs in terms of spatial and temporal discerning capabilities^{13,25,26}. On one hand, albeit GRIN lens microendoscopy retrieves calcium transients with cellular resolution, it demands a somewhat invasive surgical procedure to implant the GRIN lens into the mouse brain. Commercial GRIN lenses are relatively thick ($\geq 500 \mu\text{m}$), and oftentimes it necessitates the removal of a significant amount of brain tissue to effectively conduct the experiment^{12,26}. On the other hand, the use of thin multimode fibers (< 500 μm diameter) in photometric recordings, as well as in optogenetics experiments, has a significantly less invasive surgical procedure, which does not require any brain tissue removal, but only a careful penetration of the thin fiber through the mouse brain^{6,15,25}. It is known that the implantation of multiple multimode fibers (up to a maximum of 48 fibers²⁷) to optogenetically control and/or photometrically probe different regions in freely-behaving mouse brains is already a reality in neuroscience labs^{26–28}. However, the light wavefront propagating inside multimode fiber gets spatio-temporally scrambled due to multimodal mixing (internal scattering)^{29–31}. Generally, that is not a limitation for delivering light (optogenetics) to an ensemble of neurons in a given depth (unless one wants to probe specific neurons within the fiber field of view, FoV), but it poses a challenge for fiber photometry methods which limits the technique's potential to resolve (demix) time traces from individual neurons. Consequently, fiber photometry time traces coming from a whole population of neurons transmitted through MMF are ensemble integrated during detection, and therefore, fast single-pixel detectors are frequently chosen to optimize the detection speed and sensitivity^{15,26}. While the use of fast scientific Complementary Metal–Oxide–Semiconductor (sCMOS) cameras to simultaneously probe multiple fiber photometric signals has been demonstrated^{26,28}, the mixing between all the spatial patterns transmitted by each MMF prevented the individual retrieval of each neuron time trace²⁶.

Recently, researchers have developed novel techniques that utilize the deterministic nature of the multimode fiber transmission matrix (TM) to perform bioimaging^{30–40}. These approaches have enabled the acquisition of diffraction-limited images of fluorescently labeled brain structures and neuronal activity, even in deep brain regions (e.g., head-fixed mouse), using a multimode fiber

microendoscope³¹. To achieve this, however, an extensive characterization of MMFs transmission properties is necessary, ideally taking into account TM changes whenever the MMF fiber is bending or changing its transmission properties during an experiment, as well discussed in previous research^{32,40,41}. Consequently, while these techniques provide a minimally invasive method to obtain diffraction-limited resolution in deep brain regions, they are complex to implement and require a wavefront shaping device (e.g., spatial light modulator, SLM) to compensate for the fluorescence randomized wavefronts through a lengthy calibration procedure. Moreover, the calibration can be even more complex if the experiment is not performed in head-fixed mice, but in freely behaving mice, such as those in long-term social behavior studies^{31,32}. Finally, the use of spatial light modulators and complex distal optical devices poses an extra challenge in future use in miniaturized wireless systems.

In this article, we propose a novel approach to perform minimally invasive fiber photometry experiments disentangling single-source time traces transmitted by short and thin multimode fibers (≈ 200 μm diameter and with < 10 mm length). Our method involves the demixing of fluorescence spatio-temporal signals by applying a single post-processing step on the recorded video data of 2D scattered fluorescence patterns transmitted by the fiber. By substituting the bucket detector with a camera (i.e., a pixelated detector such as CMOS sensor), we can profit from using the spatial information of the fluorescence patterns transmitted by the multimode fiber, enabling single-source temporal activity resolution. Analysis of the recorded video is performed employing a simple unconstrained Non-Negative Matrix Factorization (NMF) algorithm that separates each spatial scattering pattern component with its corresponding temporal trace (singular trace)^{42,43}. With this approach, we show that it is possible to extract single-source time traces in fiber photometry without the need to perform any complicated calibration procedure.

Previous work from some of the authors showed that it is possible to spatio-temporally demix fluorescence scattering patterns (*speckles*) transmitted through a highly scattering media (e.g., mouse skull) by using a Non-Negative Matrix factorization (NMF) algorithm^{43,44}. The NMF algorithm relies on the premise that the input data matrix only contains non-negative values, and it has been used to decompose datasets into their representative parts or components^{42,43,45–48}. In addition, if *a priori* knowledge of the input dataset is known (e.g., sparsity, calcium transient profile, etc.), it is possible to improve the performance of NMF by adding some constraints^{49–52}. Therefore, the video data of fluorescence speckles fluctuating over time are a highly appropriate input matrix for NMF, because the superposition of these intensity signals is naturally positive, linear, and sparse due to the incoherent nature of the fluorescence process (i.e., there is no destructive interference on the propagation process of incoherent light). Based on that, one could in principle apply the same algorithm to the video data from scattering patterns that are characteristic of the light transmitted through short multimode fibers of the same length as the ones implanted in fiber photometry^{26,53–55}. It is well known that multimode fibers randomize the fluorescence wavefront propagating within it, acting as a scattering media over the fiber length due to multimodal mixing. Nevertheless, the multimode fibers (< 10 mm) typically implanted in living mice for chronic behavioral experiments are too short to generate a fully evolved speckle wavefront^{53,55}. In fact, the light wavefront that emerges from such short fibers displays a very peculiar spatial distribution of light, which is structurally mixed, but not fully spatially randomized/sparse^{53,54}. Hence, these scattering patterns cannot be considered yet a fully developed *speckle* (such as the ones in our previous work⁴³), because they still display some continuous structures whose shape depends mostly on the multimode fiber core geometry⁵⁶. Here, we call these short MMF patterns as scattering fingerprints.

In the present work, we designed a proof of principle experiment (Figure 01) and we confirmed that a simple unconstrained NMF could also disentangle the short MMFs scattering fingerprints signals and retrieve their corresponding time traces. As a consequence, one may now temporally resolve and count the number of sources with singular time traces transmitted by a minimally invasive multimode fiber. Thus, the results of this paper consist of a proof of concept on how to obtain individual time trace resolution in fiber photometry methods. Besides, we validated our approach in a more realistic condition by selectively exciting a few structurally Gad-eGFP labeled neurons in a 50 μm fixed brain slice with literature-available time traces to mimic neuronal activity. Finally, we propose a novel method for probing neuronal microendoscopic signals by simply combining a miniscope and an implantable short multimode fiber, which we called MiniDART (for Miniaturized Deep Activity Recording with high Throughput). For that, we demonstrate that the inexpensive and commercially available open-source miniscope (Open Ephys Miniscope-v4.4) has already enough sensitivity and illumination power to detect the typical intricate patterns of short MMFs. This new way of measuring individual fluorescence time traces from an ensemble of fluctuating sources profits from the short length of multimode fibers that are naturally more rigid (bending resistant) and therefore very suitable to be used in long-term freely-moving mice neuroscience experiments.

2 Results

2.1 Proof of principle using phantom samples made of 10 μm diameter fluorescent beads

To demonstrate the validity of the method, we implemented an optical setup using a digital micromirror device (DMD), which was used to generate different excitation ground truth (GT)^{43,57} activity traces for each fluorescent source (10 μm fluorescent beads \approx neuron soma size). Each source emits fluorescence that is collected and transmitted by the multimode fiber (see Figure 01 and methods for details). Upon propagating through the MMF, the fluorescence wavefront undergoes scrambling, resulting in the emergence of

fluorescence patterns upon exiting the fiber. The controlled excitation guarantees that each fluorescent source generates a fingerprint pattern whose intensity transiently fluctuates accordingly with the chosen GT time trace profile (see transient patterns in Figure 01). Thereafter, we record a video of the transient patterns that emerge from a short multimode fiber and apply the NMF to the recorded data. In Figure 02 we show the results retrieved by NMF and compared with the ground truth. The results consist of individual spatial fingerprint patterns (Figure 02e) and, most importantly, their corresponding single-activity time traces (Figure 02f) that without NMF would be mixed.

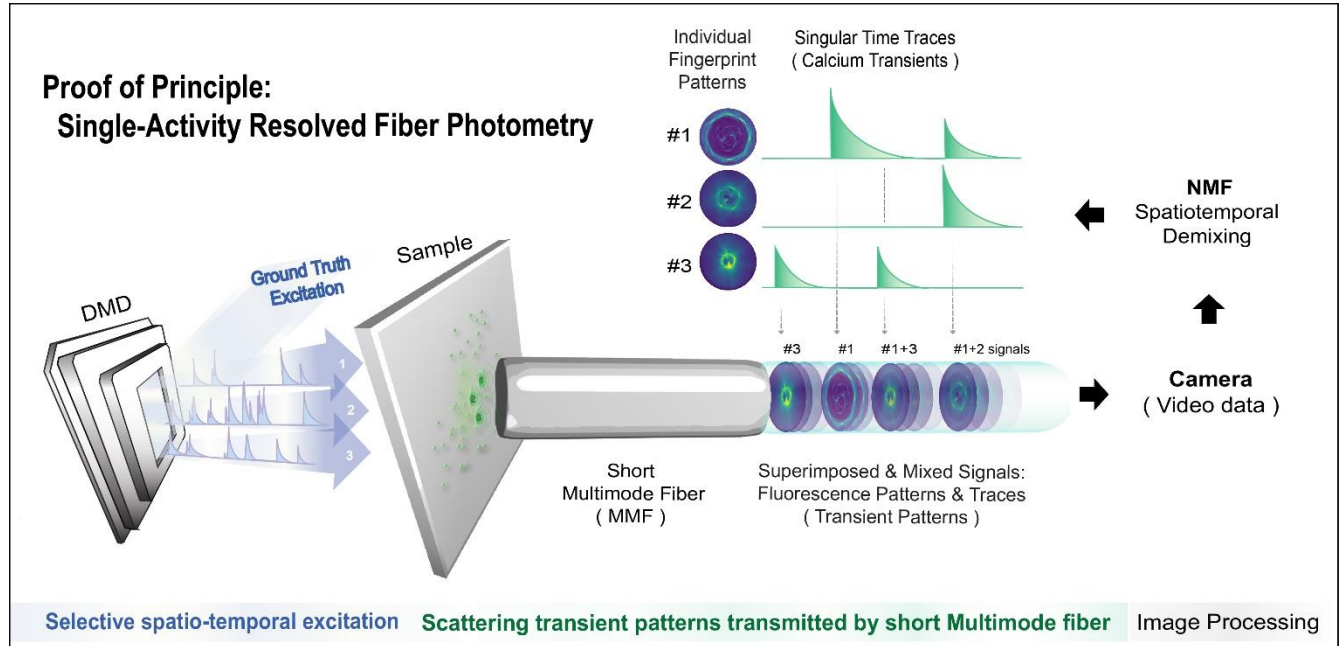


Figure 01 – Concept of single-activity resolved fiber photometry. From left to right: ground-truth excitation mimicking neuronal activity is performed by using a DMD, which can selectively excite a set of fluorescent emitters on the sample with a given time trace, likewise in ⁴³. A short (8 mm long) multimode fiber typically implanted in optogenetics or fiber photometry experiments (NA = 0.39, 200 μm core diameter, step-index fiber) is placed almost touching the sample (distance of $\approx 50 \mu\text{m}$) to collect the fluorescence dynamics of each source. Due to its proximity to the sample, the fiber's effective FoV is expected to be slightly larger than the core size. Fluorescence light inside the multimode fiber is subject to multimodal mixing during propagation, which scrambles/mixes the emitters' wavefront similarly to any scattering media. The transmitted superimposed signal consists of fluorescence transient patterns, i.e., 2D patterns that fluctuate in intensity over time. A video is recorded with a camera and a post-processing step using a spatio-temporal demixing algorithm (unconstrained NMF) is applied to disentangle the overlapped transient patterns into individual 2D spatial fingerprints and their corresponding singular time trace profiles that should match the GT excitations. For setup details, see supp info.

As can be seen in Figure 02a, the scattering patterns transmitted by the short MMF of 6 fluorescent bead sources (Figure 02c) have a significant overlap in space when all of the sources are simultaneously excited with the DMD (Figure 02a). On the other hand, whenever a fluorescent bead is excited individually, each detected spatial pattern has a very different spatial structure/morphology (see the GT scattering fingerprints in Figure 02d). After applying the unconstrained NMF on the recorded video data, the demixed spatio-temporal result by NMF had an overall good agreement with the GT. Not only the NMF retrieved well each singular temporal activity trace (Figure 02f-g), but also the individual spatial fingerprint patterns (Figure 02d-e). Since we know the GT activity, we sorted and assigned the source indexes in descending order of the correlation between their time trace obtained by the NMF and the GT. As we can see in Figure 02g, the GT-NMF temporal correlation coefficient values were high for all the first 5 beads, which were localized closer to the central region of the fiber (Figure 02c). More specifically, we obtained an average value of $\langle \delta_{g,n} \rangle = \delta_{\text{avg}} = 85.4\%$ with a standard deviation of $\text{std} = 3.6\%$ (Figure 02g). However, the NMF algorithm could not reliably recover the time trace and fluorescence patterns corresponding to bead #6 due to low SNR, probably because it was localized too far from the center, i.e. at the edge of the field of view (fiber core border, see Figure 02c), as suggested by the low intensity of GT scattering pattern (Figure 02d, index 6). In the analysis process, the input rank of NMF determines the number of components the algorithm demixes the spatio-temporal signal. When we choose an NMF's rank value higher than the real number of fluorescence sources, we obtain replicas of the scattering fingerprints and the background (see supp info), similar to what happened in a previous work⁴⁸. Thus, counting the maximum number of unique patterns demixed by NMF could be a way to count the real number of sources probed by the fiber. A more technical analysis of it can be found in the supp info.

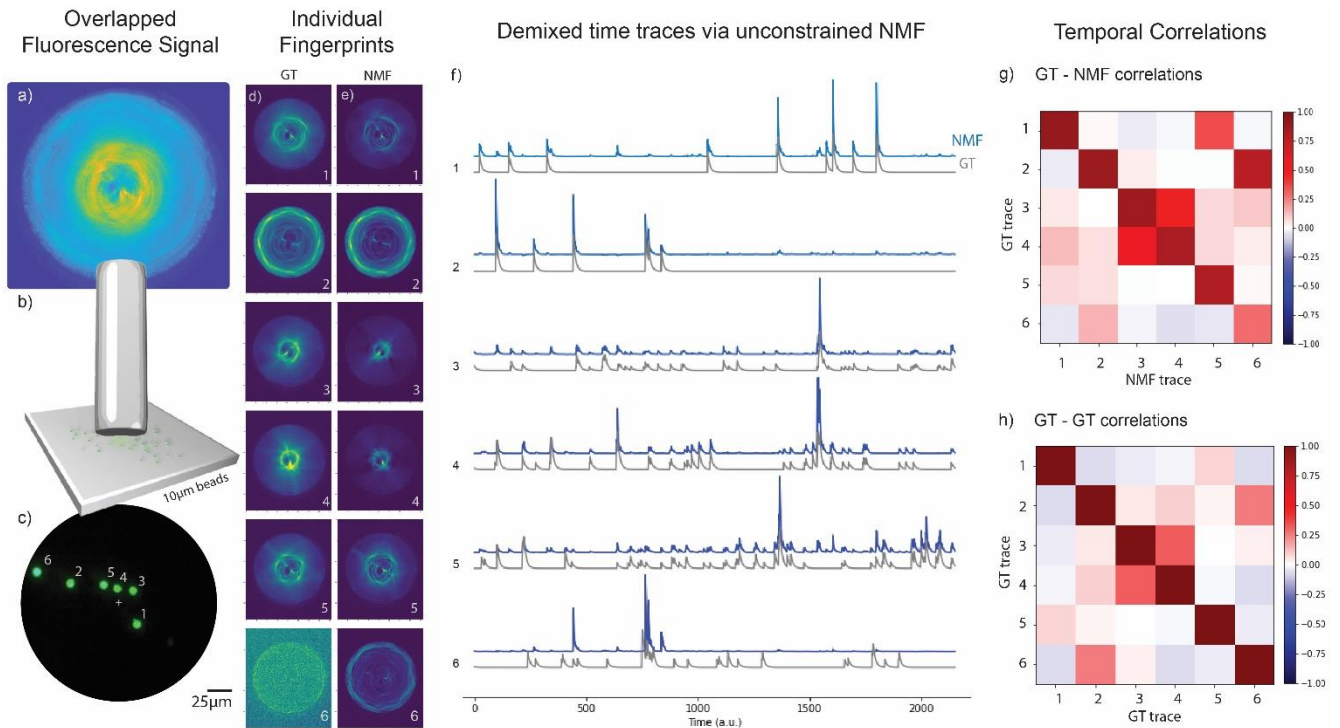


Figure 02 – Results of the proof of principle experiment. From (a) to (c) we have: (a) the fiber proximal end image of 6 fluorescent bead fingerprint patterns overlapped on the sCMOS camera chip (see methods); (b) the short MMF located at a distance of $60 \pm 10 \mu\text{m}$ from the fluorescent beads; (c) a CMOS Basler camera with the ground truth image of the sample (see supp info). (d) The ground truth (GT) fingerprint patterns were obtained from each bead when they were individually excited. (e) The fingerprint patterns obtained via NMF are to be compared with the GT patterns in d. (f) The individual temporal activity traces of the sources obtained with NMF (blue) and their corresponding GT traces (gray). The NMF trace (#6) was not recovered well by NMF since bead #6 was localized very close to the fiber core edge, therefore yielding low signal/contrast of its pattern (see GT scattering fingerprint of bead #6 in d). (g) The GT-NMF time trace correlations. The average diagonal value of the first 5 beads was $\langle \delta_{g,n} \rangle = \delta_{\text{avg}} = 85.4\%$ with $\sigma_{\delta} = 3.6\%$. To better evaluate the off-diagonal elements, we subtract them from their corresponding GT-GT coefficients. Then, we averaged the absolute values of these differences and we obtained the mean absolute error of $\zeta_{\text{avg}} = 7.06\%$ with a standard deviation of $\sigma_{\zeta} = 7.29\%$ for the first 5 beads (see supp info). (h) The GT-GT temporal trace correlation table. Importantly, the GT-GT correlation coefficients show that although each GT trace was unique in time (singular), GTs from different sources were not fully uncorrelated. For example, GT traces of beads #3 and #4 were fairly correlated ($\nu_{3,4} = \nu_{4,3} = 31.2\%$, in (h)) and had a very clear spatial overlap (see GT and NMF scattering fingerprints #3 and #4 in (d) and (e)).

2.2 Validation of the method while probing GFP-labelled neurons in a $50 \mu\text{m}$ thick fixed brain slice

We showed that our method works for a sample of fluorescent beads mimicking neuronal size and activity, however, a real GFP-labeled brain would display higher background and the labeled neurons would have a lower fluorescence signal⁴³. Therefore, in a second set of experiments, we changed our fluorescent sample to a $50 \mu\text{m}$ fixed brain slice (structurally Gad-eGFP labeled neurons, see methods for more details), and carried out the same type of GT excitation on a few selected neurons in the fiber FoV (mimicking more realistically the neuronal activity in a living brain). After recording a video of the scattering transient patterns and applying the unconstrained NMF, we confirmed again (see Figure 03) a good retrieval of the number of neurons, their scattering fingerprints (Figure 03d-e), and their individual activity traces (see Figure 03f-g and supp info). As in the previous experiment, the GT-NMF temporal trace correlation values obtained were high, with an average value of $\langle \delta_{g,n} \rangle = \delta_{\text{avg}} = 86.7\%$, and a standard deviation of $\text{std} = 2.8\%$.

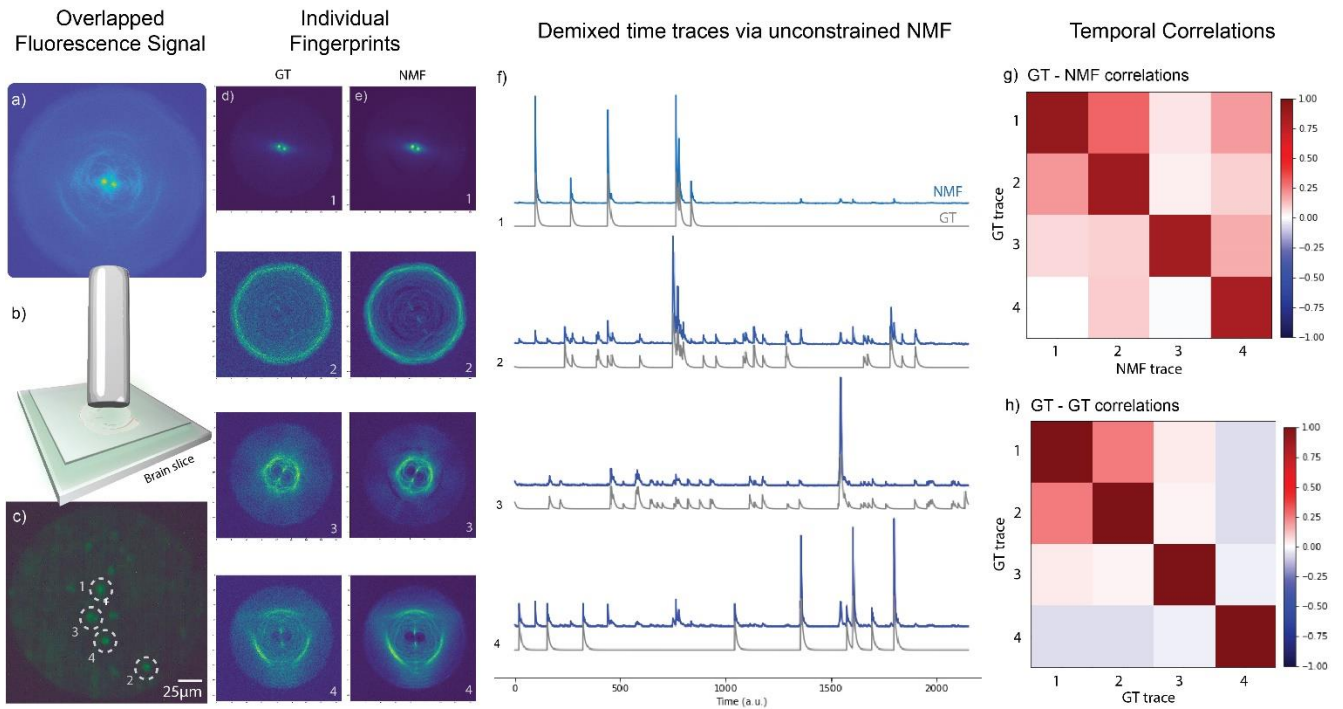


Figure 03 – Validation of the concept of single-activity resolved fiber photometry with short multimode fibers (short MMF) in a more realistic biological condition. Sample: Gad-EGFP neurons fixed in a 50 μm brain slice, sealed in between 2 coverslips to keep the humidity of the tissue (see methods). From (a) to (c) we have: (a) the fiber proximal end image of 4 neurons' fingerprint patterns spatially overlapped on the sCMOS camera chip; (b) an illustration of the short MMF placed above the top coverslip of the sample, at a distance of $\approx 60 \pm 10 \mu\text{m}$ from it; and (c) the GT image of the sample highlighting the 4 selected neurons to be excited (structurally labeled). (d) The GT fingerprint patterns are obtained from each neuron when individually excited. (e) The fingerprint patterns retrieved via NMF are in good agreement with the GT patterns in (d). (f) The demixed temporal activity traces are sorted in descending GT-NMF correlation order. Traces in blue are retrieved by NMF and temporal traces in gray are their GT. (g) The GT-NMF temporal trace correlation coefficients. The average diagonal value of the 4 neurons was $\langle \delta_{g,n} \rangle = \delta_{\text{avg}} = 86.7\%$, with standard deviation of $\sigma_{\delta} = 2.8\%$. Regarding the non-diagonal elements, the mean absolute error compared with the GT-GT coefficients was $\zeta_{\text{avg}} = 8.95\%$ with a standard deviation of $\sigma_{\zeta} = 8.02\%$ (see supp info). Again, although each GT trace was unique in time (singular), they were not fully uncorrelated as we can see in the GT-GT correlation traces (h). Interestingly, neurons #1 and #2 (i.e., the two best NMF retrieved results) were also the most temporally correlated ones in the GT excitation ($\gamma_{1,2} = \gamma_{2,1} = 25.0\%$).

2.3 Sensitivity of low-cost miniscopes in probing individual short MMF scattering fingerprints

Finally, we investigated if an inexpensive miniscope (Open Ephys Miniscope-v.4.4) would have enough sensitivity to excite and image an individual fluorescence fingerprint pattern emitted from a single fluorescent source (Figure 04a). In other words, both the LED excitation from the miniscope and the fluorescence signal from the sample would be transmitted within the short MMF before imaging. This is an important question because the miniscope has simple, inexpensive, and compact components, such as the commercial-grade CMOS detector, rather than a high-end sCMOS camera as in our proof of principle tabletop experiment (see methods). To tackle this question, we combined a miniscope with a short MMF (the MiniDART) and tested the miniscope sensitivity with a very sparse bead sample: a single fluorescent bead that we can displace laterally in the fiber FoV (see methods and Figure 04b-c). When we set the miniscope for low LED power and with no camera gain (LED = 20% corresponds to a transmitted power through the short MMF of $P_{\text{MMF}} < 10 \mu\text{W}$), it was already possible to detect short MMF scattering fingerprint patterns with very good contrast at the fastest framerate available in the miniscope control software (FPS = 30 Hz, see supp info). Interestingly, whenever raising the LED power, decreasing the framerate speed, or raising the camera gain value, the detected patterns by the miniscope got saturated, showing that the tested miniscope has already enough sensitivity to probe scattering fingerprints through short MMFs even from less bright fluorescent sources than the ones used here, especially when the fluorescent source is close to the center of the fiber core (see Figure 04a,d). At distances $d < 20 \mu\text{m}$ from the core center, the CMOS got saturated while the miniscope GUI settings were: LED power = 20% (where $\text{LED}_{\text{max}} = 100\%$, corresponding to a transmitted power through the short MMF of $P_{\text{MMF}}^{\text{max}} = 125 \mu\text{W}$), FPS = 10 Hz (where $\text{FPS}_{\text{max}} = 30 \text{ Hz}$), and Gain = 1 (where $\text{Gain}_{\text{max}} = 3.5$).

Neuronal microendoscopy with a MiniDART

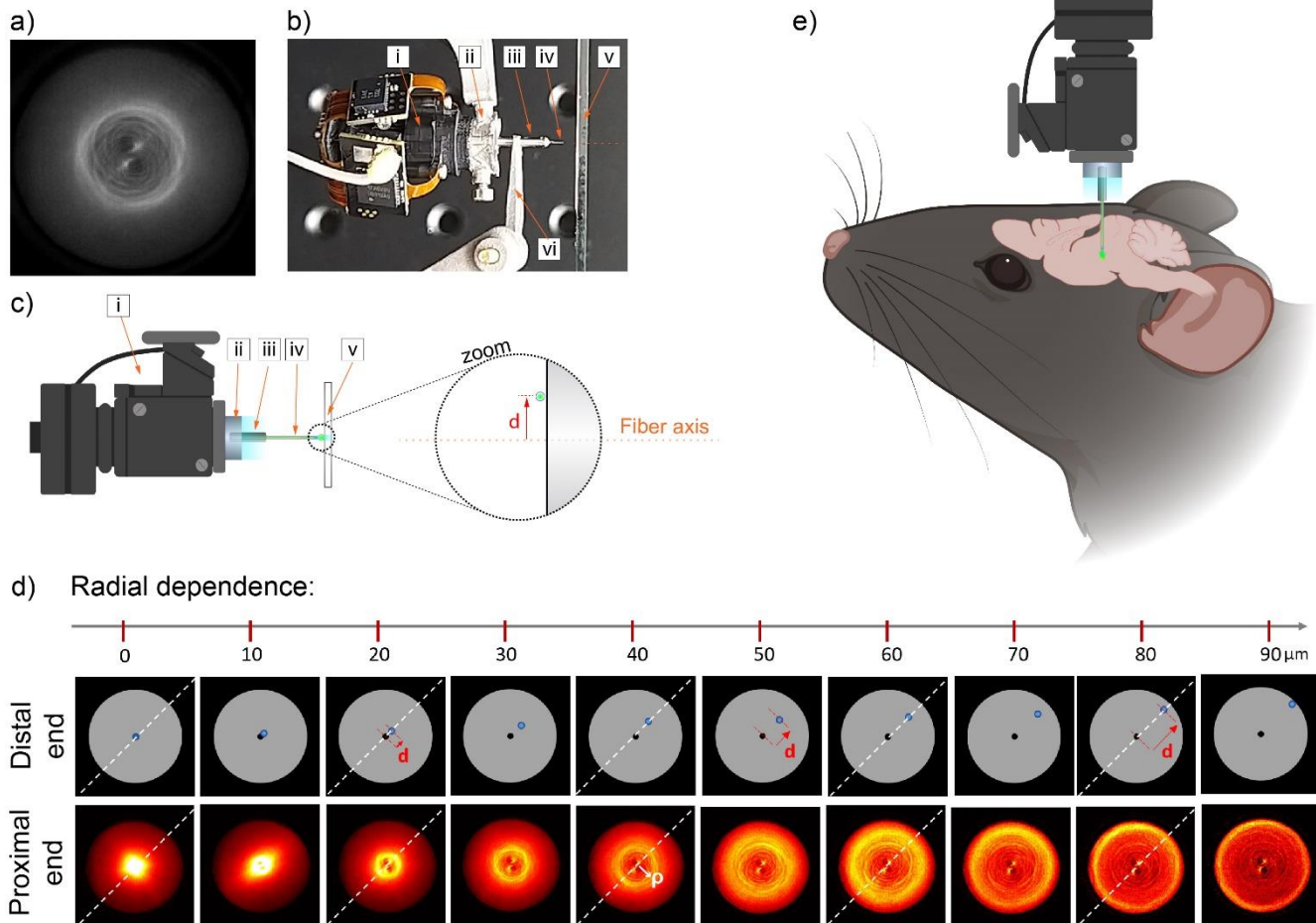


Figure 04 – Novel microendoscopy concept using a short MMF and a miniscope: the MiniDART. (a) A typical fingerprint pattern from a single-fluorescent bead ($10\ \mu\text{m}$ diameter) probed by using only the miniscope excitation and miniscope detection through the multimode fiber. (b) The experimental setup to probe scattering patterns from the short MMF includes (i) the miniscope, (ii) a customized titanium base plate (YMETRY®) to hold the miniscope, (iii) a ferrule (Thorlabs SFLC230-10) that rigidly holds the multimode fiber (iv) within it, (v) a sample consisting of a single fluorescent $10\ \mu\text{m}$ bead (spatial density $< 1\ \text{bead}/\text{cm}^2$), and (vi) a customized titanium tweezers (YMETRY®) to hold the ferrule. (c) Illustration of the experiment designed to probe the scattering pattern sensitivity from a single fluorescent source and its dependence on the source radial position in the FoV. The radial position is represented by the red vector d from the fiber axis (orange dashed line). The blue light in the illustration represents the LED excitation from the miniscope. (d) The scattering fingerprints (proximal end) morphology depending on the radial position (d) of the single-bead (blue dot, in the distal end), which was displaced every $10\ \mu\text{m}$ from the fiber main axis (black dot in the center at distal end cartoons). The bigger the distance d , the wider the diameter of the bright spiral-ring pattern (radius p in the proximal end) transmitted through the short MMF. The diagonal white dashed line is the azimuthal orientation of the vector d , which always coincides with the alignment angle of the 2 central bright points of the fingerprint patterns in the proximal end (see supp info for details). (e) The concept of doing experiments with a MiniDART device, which combines a miniscope and a short implantable multimode fiber. The system should be glued on the mouse skull with dental cement in the same way typical miniscope experiments are performed with GRIN lenses.

Fundamentally, the MiniDART is not designed for imaging or localization (like in other works that used learning algorithm methods^{53,54}). In many experiments, the relevant biological information does not depend on the shape or local position of the neurons, but mostly on the activity of each of them and their number. To extract this information, just demixing fluorescence time trace signals with NMF would be enough for relevant applications, since the number of neurons (NMF rank) could be obtained by counting the number of unique MMF fingerprints, and possibly confirmed by a *post-mortem* evaluation of the brain region right below the thin hole made by the MMF. In addition, recording the spatial fingerprints of each source would be useful for chronic experiments (to match the sources from one session to the next). However, as we can also see in Figure 04, the morphology of short MMF fingerprints provides some interesting insights into the point source position at the fiber distal end - without the need for any computational learning method. As we move a single bead laterally in a radial manner (in the x,y -plane at the fiber's distal end), a few easily interpretable geometrical properties

of the fluorescence patterns systematically change in the fiber's proximal end (Figure 04c-d). More specifically, when the bead is displaced from the center towards the fiber border (of a distance d) a bright ring (of diameter ρ) with some spiral ramifications is deterministically formed (see supp info for more details). Larger d distances yield wider rings (larger ρ , see Figure 04d). Thus, each fingerprint's bright ring diameter is encoding radial information about the bead lateral localization at the distal end. The dependence of fingerprint shape features on the individual point source position is further discussed in the supplementary information.

3 Discussion

Multimode fibers are well known to be minimally invasive microendoscopic probes that could be promptly combined with optogenetics manipulation of neuronal activity for behavioral neuroscience studies in living mice^{15,27,28,55}. It is well known from the literature that long multimode fibers (MMF length > 100 mm) could be used to transmit fluorescence activity signal and that would naturally generate a speckle wavefront due to internal multimodal mixing^{30,34,58,59}. However, as well described in wavefront shaping experiments, speckle wavefronts are extremely sensitive to fiber bending, torsion movements, and temperature changes along the fiber, which demands a long and meticulous wavefront propagation characterization (e.g., calibration using spatial light modulators, SLM) to compensate for all the changes in spatial properties of the speckles^{32,41}. In other words, there would be many experimental conditions to take into account to guarantee that the speckle patterns from each source would remain the same over time when using a long MMF as a photometric probe in freely-behaving mice experiments. That is using only a short and more stable multimode fiber for this type of application could be a very pragmatic solution.

To this end, we designed an experiment with known ground truth excitation to be able to evaluate if NMF could demix the individual spatio-temporal readouts characteristic of short MMFs. In this paper, we demonstrate that it is possible to demix such spatio-temporal signals. We used a simple and general unconstrained NMF algorithm on the video data recorded in our proof of principle experiment. It is the first time, to the best of our knowledge, that NMF is used to demix fluorescence fluctuating signals transmitted by a multimode fiber. In particular, the present work presents the proof of concept on how to obtain fluorescence activity readouts reaching single-source resolution in short multimode fibers. Since in our previous work, we already proved how to demix fluorescence speckles that are transmitted by highly scattering media (e.g., bone tissue⁴³), the same principle is also readily applied for long MMF applications too. Therefore, this work opens a promising direction to improve fiber photometry fluorescence experiments by reaching single-source temporal activity resolution.

To benefit from the short MMF's scattering fingerprint patterns and rigidity, one could directly image the proximal end of the short (implantable) MMF with a miniscope. That would be different from the typical scheme in fiber photometry, where there is an optical coupling between the transmitted light from the implantable MMF to another long MMF. In this sense, we tested and confirmed that even a low-cost miniscope would have enough LED power and CMOS speed/sensitivity to image the intricated scattering patterns transmitted by short MMFs emitted from just a single source. Both the multimode fiber and the miniscope (Open Ephys Miniscope-v4.4) are affordable and available in the market to carry out an experiment on living mice. Therefore, in this paper, we show a low-cost and simple way to expand the capacity of fiber photometry methods in resolving neuronal activity circuitry (that have already been used to investigate deep brain regions in chronic behavioral experiments in freely-behaving mice). In addition, as a minor result, we point out in Figure 04 that the short MMF scattering fingerprint morphology can have some interpretable geometry that has a relation with the source (≈ 10 μm size) localization at the distal end of the fiber. The relationship between the source localization and its fluorescence pattern shape is discussed in the supp info, but the key message for demixing is that the scattering fingerprint patterns seem to not be ambiguous depending on the source lateral position from the fiber axis.

Although computational learning tools have already been applied on short MMF scattering fingerprints to retrieve back the ground truth structural image of deep brain regions from a fixed thick brain slice^{53,54}, it is not yet proven that their approach could correctly assign the neuronal activity in living mice or any artificial condition. On the temporal resolution side, they tracked the movement of a fluorescently labeled worm in 2D with a framerate (2 Hz), which is relatively low for typical calcium transient imaging experiments performed in living mice. In the latter case, experiments are typically carried out with a framerate of at least 10 Hz (such as the one available in the miniscope DAQ software). Besides, any learning algorithm depends on the specific conditions of the training set (fiber properties, imaging optical components properties, etc.), which is less general and therefore less applicable to any other new neuroscience experiment.

Finally, we emphasize that in our method we used a very simple and general unconstrained NMF directly on the raw data, which means that there is plenty of room for performance improvement, not only optically wise (tailoring new miniscopes for this specific application) but also on the computational analysis side. On the latter, one could add biophysical-inspired constraints on the NMF algorithm (spatio-temporal priors, such as in CNMF^{51,52}) or simply add some extra data processing steps on the recorded data (e.g., matrix transformations, filtering, etc⁵¹). Indeed, it is already well known in the literature that CNMF is superior compared to NMF in demixing calcium trace signals in conventional GRIN lens imaging microendoscopy^{51,52}. Regarding the miniscope potential improvements, when we spatially binned the video recorded by our high-end sCMOS camera (tabletop experiment) until we get a similar number of FoV pixels

used in the miniscope, the retrieved results of NMF fingerprints and traces were visually indistinguishable (see supp info) compared to a non-binned analysis. This finding reinforces the idea that the current default design of the miniscope (LED power, camera speed/sensitivity, and FoV magnification) might be already enough to perform a living mouse experiment, although most pixels of the miniscope's camera chip were not used in our case (less than 1/9 of the FoV pixels were used to image a single MMF proximal end tip). Nevertheless, another way to improve the technical performance would be to design new miniscopes specifically for the application of our method, such as having a smaller FoV, with faster and even more sensitive detection (e.g., having a bigger bit-depth).

4 Conclusion

In this paper, we demonstrate how one could obtain single-source temporal activity resolution in fiber photometry experiments that use multimode fibers as a microendoscopic probe. Besides, we show that the currently available low-cost miniscope has enough sensitivity to image directly the implantable short MMF scattering fingerprints so that it could be advantageous for long-term microendoscopic studies in freely-behaving animals due to the rigidity of short fibers (< 10 mm). Therefore, we believe that this work can open a whole new avenue for novel and affordable minimally invasive deep brain microendoscopic studies to probe (potentially several) deep brain regions in freely-behaving animals, including experiments that could be conveniently coupled with optogenetics approaches like already been implemented in the neuroscience community.

5 Methods

Proof of principle setup:

The proof of principle setup is visually illustrated and fully described in the supp info.

Fiber-ferrule preparation:

The multimode fiber was purchased from Thorlabs (FT200UMT, NA = 0.39, $200 \pm 5 \mu\text{m}$ core diameter, $225 \pm 5 \mu\text{m}$ cladding diameter). Around 10 cm of the fiber was initially cleaved with a ruby blade (Thorlabs, S90R), and the quality of the cleaved edge was inspected with a stereomicroscope (LEICA A60F, maximum magnification 30x). The fiber was glued within a 1.25 mm wide and 6 mm long stainless-steel ferrule (Thorlabs SFLC230-10, $230 \pm 10 \mu\text{m}$ bore diameter) using an ultraviolet curing glue (Norland optical adhesive 81) so that the cleaved end was chosen to be the distal end of the fiber (with 2mm of it sticking out of the ferrule). The excess of the fiber on the other end (proximal end) was cut close to the ferrule edge and then sequentially polished (KRELLTECH NOVA device) with 3 different silicon carbide polishing disks with gradually descending roughness (30 mm, 3 mm, 0.3 mm, PSA 4'' polishing disks from KRELLTECH). The quality of the polished end (proximal end of the fiber) was verified with the LEICA A60F stereomicroscope. We used a customized titanium tweezer and baseplate to hold the ferrule and the miniscope respectively (YMETRY®).

Preparation of the fluorescent bead sample:

In the proof of principle experiments, the samples consisted of randomly distributed fluorescent beads on borosilicate glass (22x40 mm cover glass, thickness Nb.1.5, purchased from VWR). An aliquot (100x diluted in milli-Q water) of the polystyrene (PS) particles aqueous suspension (PS - FluoGreen - Fi226 – 1mL, $10.23 \pm 0.13 \mu\text{m}$ size, abs/em = 502/518 nm, purchase from microParticles GmbH, Germany) was used to randomly distribute the beads on the cover glass. The beads' size was chosen to have similar size to typical neuron soma probed in calcium imaging experiments. Besides, the emission spectrum of the beads is close to the common GFP calcium indicators. For the single-bead sample, a more diluted aliquot (from 10^6 to 10^7 times dilution) was used to guarantee a very spatially sparse bead sample with density $\leq 1 \text{ bead}/\text{cm}^2$, so that there would be only a single bead throughout the Fiber FoV whenever translating the bead laterally in the miniDART experiment (easily inspected by the miniscope itself without the fiber).

Preparation of the fixed brain slice sample:

The work includes data from one GAD65-EGFP transgenic mouse (heterozygote; male; aged 6 months) expressing EGFP in Gad65-positive interneurons in the brain and spinal cord. All procedures involving this animal complied with French and European legislations relative to the protection of animals used for experimental and other scientific purposes (2010/63/UE) and were approved by the "Charles Darwin" institutional ethics committee under the direction of the French National Committee of Ethical Reflection on Animal Experimentation under authorization number APAFIS 26667. The mouse was euthanized by cervical dislocation performed on the terminally anesthetized animal (5% isoflurane for 5 minutes in an induction chamber) and the brain was quickly removed from the skull and immediately transferred into a fixation solution (4% paraformaldehyde; pH 6.9 buffered; Sigma-Aldrich #1004965000). After 12 h at 5° the brain was transferred into phosphate-buffered saline (PBS) and cut into tangential slices of 50 to 100 μm thickness using a vibratome (Leica VT1000). Obtained slices were stored in multi-well plates with PBS and assessed with a fluorometric microscope before the experiment with the DMD.

NMF Analysis in Python:

The raw video data [2D image, time] was reshaped to a 2D matrix [1D image, time] to fit the input format of NMF. We used the scikit-learn decomposition NMF package freely available online (Python) ^{44,60}. In the code pipeline, an optional pre-processing step was added, which included an option for pixel binning (see supp info). The NMF parameters chosen ignored the additional parametric terms that are introduced to account for the sparsity of the data. The parameters chosen were: *init* = 'nndsvd', *random_state* = 0, *max_iter* = 3000, *solver* = 'cd', *l1_ratio* = 1, *beta_loss* = 2, *alpha_W* = 0, *alpha_H* = 0. The parameter *n_components* (which is the chosen NMF rank) changes depending on the experiment and a more detailed discussion about how to choose this value can be found in the supp info. In particular, the rank used in Figure O2 was $\text{rank}_{\text{Fig2}}=9$ (explained in the supp info), and the rank for Figure O3 was $\text{rank}_{\text{Fig3}}=5$. The results of Figure O2 with different ranks are illustrated in the supp info.

The non-diagonal coefficients mean and standard deviation of the temporal correlation results:

The matrix of the non-diagonal elements $\zeta = \zeta_{i \neq j}$, where each element is the mean absolute error value between GT-NMF and GT-GT coefficients is detailed described in the supp info. The mean absolute error (MAE) value of a given element in $\zeta_{i \neq j}$ is given by:

$$MAE_{i,j} = |\mathbf{v}_{i,j} - \boldsymbol{\gamma}_{i,j}|$$

Where, $\mathbf{v}_{i,j}$ is the (i,j) non-diagonal coefficient of GT-NMF temporal correlations, and is $\boldsymbol{\gamma}_{i,j}$ the corresponding (i,j) non-diagonal coefficient of the GT-GT temporal correlations. The average value (ζ_{avg}) of all these non-diagonal elements and the standard deviation (σ) is given by:

$$\zeta_{avg} = \text{mean}(\zeta_{i \neq j}) = \frac{1}{2(N_s - 1)} \left(\sum_{i \neq j}^{N_s-1} |\mathbf{v}_{i,j} - \boldsymbol{\gamma}_{i,j}| \right)$$
$$\sigma_{\zeta} = \text{std}(\zeta_{i \neq j})$$

Where N_s is the total number of sources. These two values ($\zeta_{avg} \pm \sigma_{\zeta}$), together with the diagonal values ($\delta_{avg} \pm \sigma_{\delta}$), give us an estimation of whole experiment quality since ($\zeta_{avg} \pm \sigma_{\zeta}$) should ideally approach to zero.

6 Acknowledgments

The authors are grateful to Serena Bovetti, Stefano Zucca, and Laurent Bourdieu for productive discussions about the applications of the concept to in-vivo imaging. We are very thankful to Walther Akemann for the mouse brain extraction and fixation. In addition, we are grateful to Guillaume Dugué, Thomas Pujol, Arnaud Leclercq, and Maurice Debray for the fiber-ferrule assembly discussions and technical support (Lab. Kastler Brossel and IBENS' FabLab facilities, the latter which received support from the Fédération pour la Recherche sur le Cerveau - Rotary International France (2018)). The authors acknowledge the funding sources HFSP, SMARTIES, and France's Agence Nationale de la Recherche (ANR). The project is funded thanks to HFSP project N°RGP0003/2020. S.G. acknowledges support from H2020 European Research Council (724473 SMARTIES). C.V. acknowledges support from ANR (ANR-19-CE37-0007-02).

7 Author contributions

C.M. and S.G. conceived the idea. C.V.R. adapted the setup and performed the optical experiments, prepared the samples, adapted the code and performed the NMF analysis, and wrote the article. C.M. built the excitation ground-truth part of the setup (DMD alignment) and wrote the Matlab control code. F.S. wrote the core code in Python for the NMF analysis. E.B. and C.V.R. assembled fiber-ferrules and performed experiments with the MiniDART. C.V. and S.G. supervised and initiated the project. All authors discussed the results and commented on the paper.

8 Competing interests

The authors declare no competing interests.

9 References

1. Akemann, W. *et al.* Fast optical recording of neuronal activity by three-dimensional custom-access serial holography. *Nat Methods* **19**, 100–110 (2022).
2. Faini, G. *et al.* Ultrafast light targeting for high-throughput precise control of neuronal networks. *Nat Commun* **14**, 1888 (2023).

3. James Sofroniew, N., Flickinger, D., King, J. & Svoboda, K. A large field of view two-photon mesoscope with subcellular resolution for in vivo imaging. (2016) doi:10.7554/eLife.14472.001.
4. Hontani, Y., Xia, F. & Xu, C. *Multicolor three-photon fluorescence imaging with single-wavelength excitation deep in mouse brain*. *Sci. Adv* vol. 7 <http://spectra.arizona.edu/>. (2021).
5. Meng, C. *et al.* Spectrally Resolved Fiber Photometry for Multi-component Analysis of Brain Circuits. *Neuron* **98**, 707-717.e4 (2018).
6. Yizhar, O., Fenno, L. E., Davidson, T. J., Mogri, M. & Deisseroth, K. Optogenetics in Neural Systems. *Neuron* vol. 71 9–34 Preprint at <https://doi.org/10.1016/j.neuron.2011.06.004> (2011).
7. Shoham, S. Optogenetics meets optical wavefront shaping. *Nature Methods* vol. 7 798–799 Preprint at <https://doi.org/10.1038/nmeth1010-798> (2010).
8. Emiliani, V., Cohen, A. E., Deisseroth, K. & Häusser, M. All-optical interrogation of neural circuits. *Journal of Neuroscience* vol. 35 13917–13926 Preprint at <https://doi.org/10.1523/JNEUROSCI.2916-15.2015> (2015).
9. Szabo, V., Ventalon, C., De Sars, V., Bradley, J. & Emiliani, V. Spatially selective holographic photoactivation and functional fluorescence imaging in freely behaving mice with a fiberscope. *Urology* **84**, 1157–1169 (2014).
10. Wang, W., Kim, C. K. & Ting, A. Y. Molecular tools for imaging and recording neuronal activity. *Nature Chemical Biology* vol. 15 101–110 Preprint at <https://doi.org/10.1038/s41589-018-0207-0> (2019).
11. Zhao, C. *et al.* Miniature three-photon microscopy maximized for scattered fluorescence collection. *Nat Methods* (2023) doi:10.1038/s41592-023-01777-3.
12. Resendez, S. L. *et al.* Visualization of cortical, subcortical and deep brain neural circuit dynamics during naturalistic mammalian behavior with head-mounted microscopes and chronically implanted lenses. *Nat Protoc* **11**, 566–597 (2016).
13. Resendez, S. L. & Stuber, G. D. In vivo calcium imaging to illuminate neurocircuit activity dynamics underlying naturalistic behavior. *Neuropsychopharmacology* vol. 40 238–239 Preprint at <https://doi.org/10.1038/npp.2014.206> (2015).
14. Grienberger, C. & Konnerth, A. Imaging Calcium in Neurons. *Neuron* vol. 73 862–885 Preprint at <https://doi.org/10.1016/j.neuron.2012.02.011> (2012).
15. Gunaydin, L. A. *et al.* Natural neural projection dynamics underlying social behavior. *Cell* **157**, 1535–1551 (2014).
16. Ghosh, K. K. *et al.* Miniaturized integration of a fluorescence microscope. *Nat Methods* **8**, 871–878 (2011).
17. Aharoni, D. & Hoogland, T. M. Circuit investigations with open-source miniaturized microscopes: Past, present and future. *Frontiers in Cellular Neuroscience* vol. 13 Preprint at <https://doi.org/10.3389/fncel.2019.00141> (2019).
18. Ziv, Y. *et al.* Long-term dynamics of CA1 hippocampal place codes. *Nat Neurosci* **16**, 264–266 (2013).
19. Cai, D. J. *et al.* A shared neural ensemble links distinct contextual memories encoded close in time. *Nature* **534**, 115–118 (2016).

20. Eriksson, D. *et al.* Multichannel optogenetics combined with laminar recordings for ultra-controlled neuronal interrogation. *Nat Commun* **13**, (2022).
21. Wang, Y., DeMarco, E. M., Witzel, L. S. & Keighron, J. D. A selected review of recent advances in the study of neuronal circuits using fiber photometry. *Pharmacology Biochemistry and Behavior* vol. 201 Preprint at <https://doi.org/10.1016/j.pbb.2021.173113> (2021).
22. Legaria, A. A. *et al.* Fiber photometry in striatum reflects primarily nonsomatic changes in calcium. *Nat Neurosci* **25**, 1124–1128 (2022).
23. Patel, A. A., McAlinden, N., Mathieson, K. & Sakata, S. Simultaneous Electrophysiology and Fiber Photometry in Freely Behaving Mice. *Front Neurosci* **14**, (2020).
24. Paukert, M. *et al.* Norepinephrine controls astroglial responsiveness to local circuit activity. *Neuron* **82**, 1263–1270 (2014).
25. Li, Y., Liu, Z., Guo, Q. & Luo, M. Long-term Fiber Photometry for Neuroscience Studies. *Neurosci Bull* **35**, 425–433 (2019).
26. Girven, K. S. & Sparta, D. R. Probing Deep Brain Circuitry: New Advances in in Vivo Calcium Measurement Strategies. *ACS Chemical Neuroscience* vol. 8 243–251 Preprint at <https://doi.org/10.1021/acscchemneuro.6b00307> (2017).
27. Sych, Y., Chernysheva, M., Sumanovski, L. T. & Helmchen, F. High-density multi-fiber photometry for studying large-scale brain circuit dynamics. *Nat Methods* **16**, 553–560 (2019).
28. Kim, C. K. *et al.* Simultaneous fast measurement of circuit dynamics at multiple sites across the mammalian brain. *Nat Methods* **13**, 325–328 (2016).
29. Rahmani, B. *et al.* Learning to image and compute with multimode optical fibers. *Nanophotonics* vol. 11 1071–1082 Preprint at <https://doi.org/10.1515/nanoph-2021-0601> (2022).
30. Li, S., Horsley, S. A. R., Tyc, T., Čižmár, T. & Phillips, D. B. Memory effect assisted imaging through multimode optical fibres. *Nat Commun* **12**, (2021).
31. Stibůrek, M. *et al.* 110 μm thin endo-microscope for deep-brain in vivo observations of neuronal connectivity, activity and blood flow dynamics. *Nat Commun* **14**, 1897 (2023).
32. Ohayon, S., Caravaca-Aguirre, A., Piestun, R. & DiCarlo, J. J. Minimally invasive multimode optical fiber microendoscope for deep brain fluorescence imaging. *Biomed Opt Express* **9**, 1492 (2018).
33. Singh, S., Labouesse, S. & Piestun, R. Tunable Mode Control Through Myriad-Mode Fibers. *JOURNAL OF LIGHTWAVE TECHNOLOGY* **39**, (2021).
34. Singh, S., Labouesse, S. & Piestun, R. Multiview Scattering Scanning Imaging Confocal Microscopy Through a Multimode Fiber. *IEEE Trans Comput Imaging* **9**, 159–171 (2023).
35. Schmidt, C. C., Turcotte, R., Booth, M. J. & Emptage, N. J. Repeated imaging through a multimode optical fiber using adaptive optics. *Biomed Opt Express* **13**, 662 (2022).
36. Turcotte, R., Schmidt, C. C., Booth, M. J. & Emptage, N. J. Volumetric two-photon fluorescence imaging of live neurons using a multimode optical fiber. *Opt Lett* **45**, 6599 (2020).

37. Turcotte, R., Sutu, E., Schmidt, C. C., Emptage, N. J. & Booth, M. J. Deconvolution for multimode fiber imaging: modeling of spatially variant PSF. *Biomed Opt Express* **11**, 4759 (2020).
38. Lee, S.-Y., Parot, V. J., Bouma, B. E. & Villiger, M. Confocal 3D reflectance imaging through multimode fiber without wavefront shaping. *Optica* **9**, 112 (2022).
39. Sato, M. *et al.* In vivo rat brain imaging through full-field optical coherence microscopy using an ultrathin short multimode fiber probe. *Applied Sciences (Switzerland)* **9**, (2019).
40. Cao, H., Čižmár, T., Turtaev, S., Tyc, T. & Rotter, S. Controlling light propagation in multimode fibers for imaging, spectroscopy and beyond. (2023).
41. Resisi, S., Viernik, Y., Popoff, S. M. & Bromberg, Y. Wavefront shaping in multimode fibers by transmission matrix engineering. *APL Photonics* **5**, (2020).
42. Lee, D. D. & Seung, H. S. Learning the parts of objects by non-negative matrix factorization. *Nature* **401**, 788–791 (1999).
43. Moretti, C. & Gigan, S. Readout of fluorescence functional signals through highly scattering tissue. *Nat Photonics* **14**, 361–364 (2020).
44. Soldevila, F. *et al.* Functional imaging through scattering medium via fluorescence speckle demixing and localization. (2023).
45. Anderson, A. *et al.* Non-negative matrix factorization of multimodal MRI, fMRI and phenotypic data reveals differential changes in default mode subnetworks in ADHD. *NeuroImage* vol. 102 207–219 Preprint at <https://doi.org/10.1016/j.neuroimage.2013.12.015> (2014).
46. Gillis, N. The Why and How of Nonnegative Matrix Factorization. *arxiv.org* (2014) doi:<https://doi.org/10.48550/arXiv.1401.5226>.
47. Lee, D. D. & Seung, H. S. Algorithms for Non-negative Matrix Factorization. in *NIPS'00: Proceedings of the 13th International Conference on Neural Information Processing Systems* (2000).
48. Boniface, A., Dong, J. & Gigan, S. Non-invasive focusing and imaging in scattering media with a fluorescence-based transmission matrix. *Nat Commun* **11**, (2020).
49. Hoyer PATRIKHoyer, P. O. *Non-negative Matrix Factorization with Sparseness Constraints. Journal of Machine Learning Research* vol. 5 <http://cbcl.mit.edu/cbcl/software-datasets/FaceData2.html> (2004).
50. Kim, H. & Park, H. Sparse non-negative matrix factorizations via alternating non-negativity-constrained least squares for microarray data analysis. *Bioinformatics* **23**, 1495–1502 (2007).
51. Zhou, P. *et al.* Efficient and accurate extraction of in vivo calcium signals from microendoscopic video data. *Elife* **7**, (2018).
52. Pnevmatikakis, E. A. *et al.* Simultaneous Denoising, Deconvolution, and Demixing of Calcium Imaging Data. *Neuron* **89**, 285 (2016).
53. Guo, R. *et al.* Scan-less machine-learning-enabled incoherent microscopy for minimally-invasive deep-brain imaging. *Opt Express* **30**, 1546 (2022).

54. Mitra, E., Guo, R., Nelson, S., Nagarajan, N. & Menon, R. Computational microscopy for fast widefield deep-tissue fluorescence imaging using a commercial dual-cannula probe. *Optics Continuum* **1**, 2091 (2022).
55. Cui, G. *et al.* Deep brain optical measurements of cell type-specific neural activity in behaving mice. *Nat Protoc* **9**, 1213–1228 (2014).
56. OKAMOTO, K. *Fundamentals of Optical Waveguides*. (Elsevier, 2006). doi:10.1016/B978-0-12-525096-2.X5000-4.
57. Chen, T. W. *et al.* Ultrasensitive fluorescent proteins for imaging neuronal activity. *Nature* **499**, 295–300 (2013).
58. Plöschner, M., Tyc, T. & Čížmár, T. Seeing through chaos in multimode fibres. *Nat Photonics* **9**, 529–535 (2015).
59. Defienne, H., Barbieri, M., Walmsley, I. A., Smith, B. J. & Gigan, S. Two-photon quantum walk in a multimode fiber. *Sci Adv* **2**, (2016).
60. sklearn.decomposition.NMF. <https://scikit-learn/stable/modules/generated/sklearn.decomposition.nmf.html> (2023).

Demixing fluorescence time traces transmitted by multimode fibers

Caio Vaz Rimoli^{1,2*}, Claudio Moretti¹, Fernando Soldevila¹, Enora Brémont²,
Cathie Ventalon^{2*}, Sylvain Gigan^{1*}

¹Laboratoire Kastler Brossel, ENS-Universite PSL, CNRS, Sorbonne Universite, College de France, 24 Rue Lhomond, Paris, F-75005, France.

²IBENS, Departement de Biologie, Ecole Normale Superieure, CNRS, Inserm, PSL Research University, 46 Rue d'Ulm, Paris, F-75005, France.

SUPPLEMENTARY INFORMATION

• Supplementary materials - list of contents:

- Supplementary Information 01 – The proof of principle setup
- Supplementary Information 02 – Estimating the number of fluorescence sources with NMF: the NMF rank study
- Supplementary Information 03 – The miniscope detection sensitivity to a single source
- Supplementary Information 04 – Pattern shape dependence on symmetrically positioned beads (with miniscope)
- Supplementary Information 05 – NMF analysis test when binning the image
- Supplementary Information 06 – Comparing GT-NMF and GT-GT correlation coefficients

Supp info 01: the proof of principle optical setup

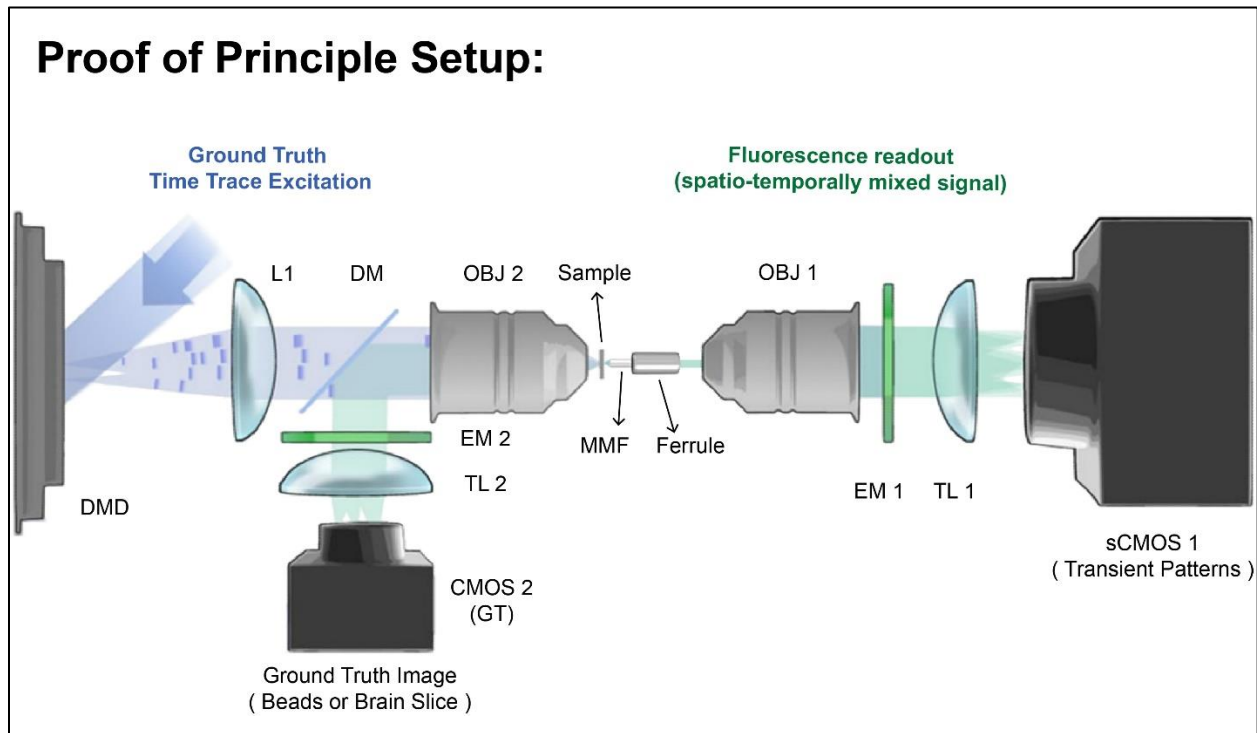


Figure S01 - The proof of principle optical setup. A 473 nm blue laser (LSR-0473-PFM-00100-01, Laserglow Technologies) illuminates a digital micromirror device surface (DMD from Texas Instruments: DLP LightCrafter 6500, same as ⁴³), that was used to create the ground truth (GT) excitation of each fluorescence source present in the sample plane (see sample details in the methods). A tube lens (L1, LA1708-A, Thorlabs) and the lower objective OBJ 2 (Plan-NEOFLUAR × 20 0.5 NA, Zeiss) were used in the excitation path. For the ground truth excitation, genetically encoded calcium indicator (GECI) traces were obtained from neuronal recordings available in the literature, as we did before in previous experiments ^{43,57}. After excitation, the fluorescent signal propagated through the short multimode fiber (see fiber-ferrule preparation details in the methods) and the fluctuating fluorescent scattering fingerprints on the tip of the fiber were imaged onto a scientific complementary metal-oxide-semiconductor (sCMOS) camera (Iris 15 sCMOS, Teledyne Photometrics) by a microscope objective (OBJ 1, RMS10X PLAN ACHROMAT 0.25NA,

Olympus) and a tube lens (TL 1). An emission bandpass filter (MF530-43, Thorlabs) was used in the detection path to block the blue excitation light. In addition, the system has a control path to image the fluorescence sample directly, so that it would be possible to obtain the ground truth image of the sample without passing through the fiber. This is done by imaging the backpropagating fluorescent light from the sample in reflection mode. For this path, a dichroic beam splitter (DM, FF496-SDi01, Semrock) was used to collect the fluorescent signal in reflection and the sample plane was imaged onto a CMOS camera (ACE2014-55um, Basler) after another tube lens (TL 2).

Supp info 02: estimating the number of fluorescence sources with NMF: the NMF rank study

The rank of NMF sets the number of components the NMF will demix from the video data (number of fingerprints and their corresponding time traces)^{42-44,48}. In the experiment of Figure 02, we probed 6 beads in the FoV. In such case, because we know the number of sources, an expected good rank number (R_{expected}) as an input in NMF would be: $R_{\text{expected}} = 7$, because there were 6 beads + 1 background signal ($R_{\text{expected}} = N_{\text{beads}} + 1_{\text{bgd}}$). In a neuroscience experiment, one might not know *a priori* the number of the sources (neurons) one is probing, hence the input rank value on the NMF algorithm is not evident. However, one could still evaluate how well NMF performs to minimize the difference between the product of the two factorized spatial (W) and temporal (H) matrices and the original video matrix (X) with different rank values. The fidelity plot is shown in Figure S02-i. There, the residual error gradually decreases until reaching stabilized values, similar to a plateau (e.g., for rank values higher than 9). The curve profile changes more drastically its curvature around rank 4 and starts to stabilize around the expected rank $R_{\text{expected}} = 7$. Therefore, one could immediately make a rough estimation of the number of sources by just calculating the fidelity of NMF.

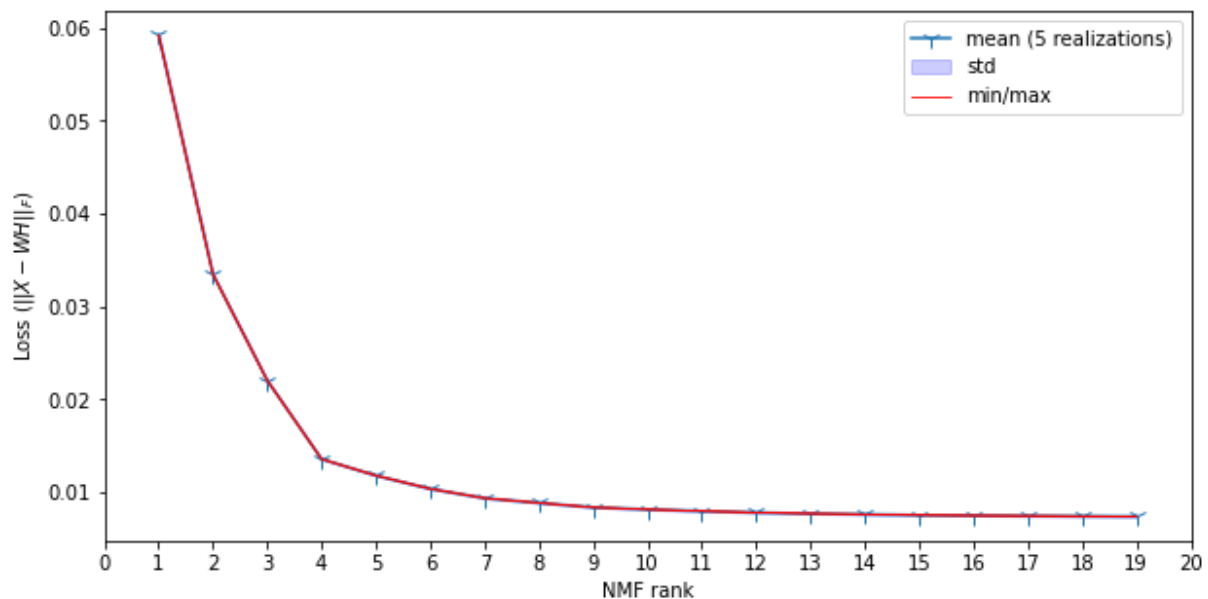


Figure S02-i – Residual error estimation (fidelity plot) for NMF with different factorization ranks. The sample used here is the same as in Figure 02 and contains 6 beads. One might see that the fidelity curve changes its curvature when the tested rank values gets closer to the GT expected rank (6 beads + 1 background). After that, the NMF performance slowly reaches a plateau. For large NMF rank values, the extra fingerprints and time traces obtained are replicas of the GT signal. NMF model parameters were the same as methods, only changing the rank value. Mean value and standard deviations (std) over 5 realizations with 3000 interactions.

However, by investigating more closely these NMF results for ranks between 4 and 10, one might be able to count the number of individual sources with more precision. This is because the extra components are due to NMF forcing to split a single signal (fingerprint and time trace) into two or more positive signals. As a consequence, we expect to obtain fingerprint replicas of the bead patterns and background. For lower ranks, signal from individual sources can be superimposed with data from other sources or with the background. For example, in when we chose rank $R = 4$, the background signal is still mixed with some of the fluorescent bead signal (see Figure S02-ii). In such case, we retrieved relatively well the signal of 3 sources (there is some cross talk between bead 3 and the bead 4), but we lost the remaining ones.

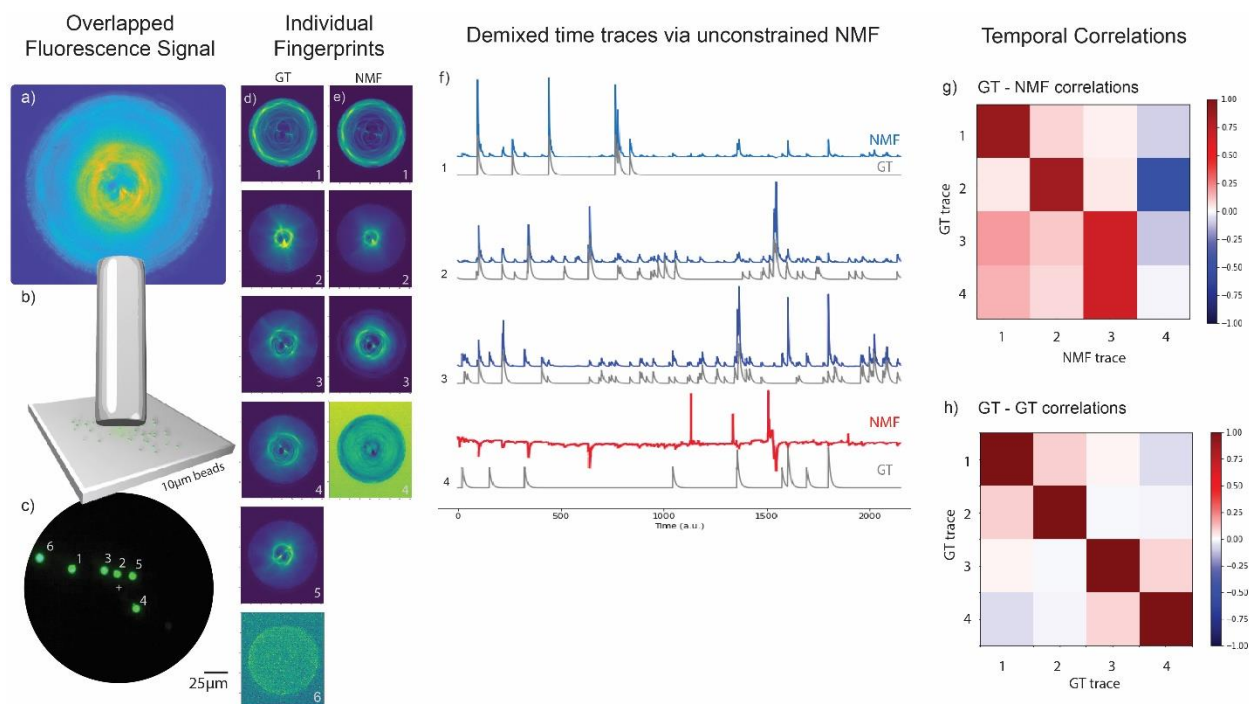


Figure S02-ii – Results of the proof of principle experiment, analyzed when we the input rank of NMF is $R = 4$. From (a) to (c) we have: (a) the fiber proximal end image of 6 fluorescent bead fingerprint patterns overlapped on the sCMOS camera chip; (b) the short MMF located at a distance of $60 \pm 10 \mu\text{m}$ from the fluorescent beads; (c) a CMOS Basler camera with the ground truth image of the sample. (d) The ground truth (GT) fingerprint patterns. (e) The fingerprint patterns obtained via NMF with rank 4. (f) The individual temporal activity traces of the sources obtained with NMF (blue) and their corresponding GT traces (gray). The red NMF trace (#4) is mainly background superimposed with the time trace activity of the other sources. (g) The Ground truth (GT) – NMF time trace correlations. The average diagonal value of the first 3 beads was $\langle \delta_{g,n} \rangle = \delta_{\text{avg}} = 81.3\%$ with standard deviation of $\sigma_{\delta} = 8.9\%$. (h) The GT-GT temporal trace correlations coefficients.

For rank $R = 7$, we did retrieve well 5 unique fingerprints and their corresponding time traces, but we did not retrieve well the signal from bead #6 mostly due low SNR ratio. When using a higher rank and sorting the most correlated NMF time traces to the GTs, the background temporal correlations were higher than the time trace signal of the bead itself (see red time trace NMF curve in Figure S02-iii). This result suggests that bead #6 was still embedded in the background for rank $R=7$.

For higher ranks than the expected one ($R > 7$), we start to split the signal of the source time traces, but also from the background (see replicas in Figure S02-iv). For NMF rank #9 (see Figure O2) and beyond, NMF always managed to find the hidden signal of bead #6 in the background component, which was correlating more with the GT of bead #6 than the background itself.

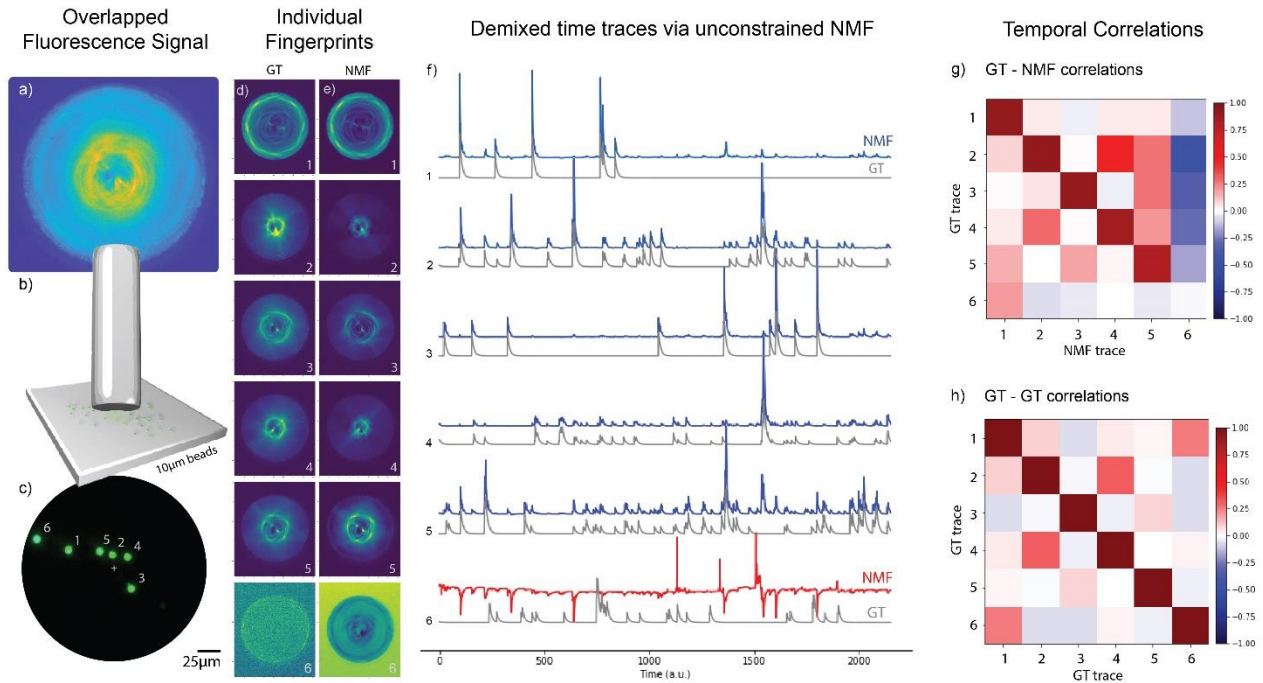


Figure S02-iii – Results of the proof of principle experiment, when NMF rank $R = 7$. From (a) to (c) we have: (a) the fiber proximal end image of 6 fluorescent bead fingerprint patterns overlapped on the sCMOS camera chip; (b) the short MMF located at a distance of $60 \pm 10 \mu\text{m}$ from the fluorescent beads; (c) a CMOS Basler camera with the ground truth image of the sample. (d) The ground truth (GT) fingerprint patterns. (e) The fingerprint patterns obtained with the NMF. (f) The individual temporal activity traces of the sources obtained with NMF (blue) and their corresponding GT traces (gray). The red NMF trace (#6) was not recovered well by NMF since bead #6 was localized very close to the fiber core edge, therefore yielding low signal/contrast of its pattern (see GT scattering fingerprint of bead #6 in d). (g) The Ground truth (GT) – NMF time trace correlations. The average diagonal value of the first 5 beads was $\langle \delta_{g,n} \rangle = \delta_{\text{avg}} = 88\%$ with standard deviation of $\sigma_{\delta} = 4\%$. (h) The GT-GT temporal trace correlation coefficients. The GT-GT correlation coefficients show that GTs from different sources were not fully uncorrelated, although each GT trace was unique in time (singular). For example, GT traces of beads #2 and #4 were fairly temporally correlated ($\gamma_{2,4} = \gamma_{4,2} = 31.2\%$, in (h)) and had a very clear spatial overlap (see GT and NMF scattering fingerprints #2 and #4 in (d) and (e)).

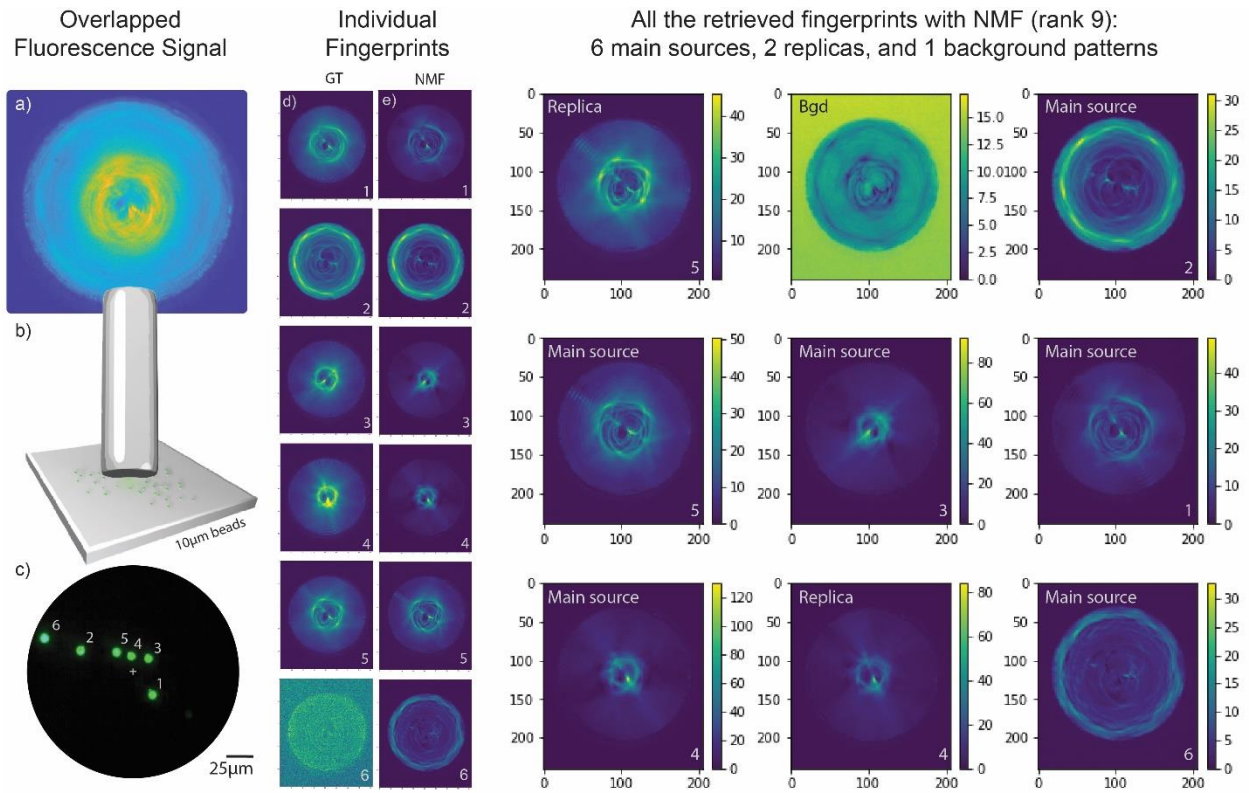


Figure S02-iv – All the fingerprint results of the proof of principle experiment, when NMF rank $R = 9$ (same as Figure O2). When rank is $R = 9$, the NMF demixes the data video in 6 main sources, 2 replicas, and 1 background (bgd).

Supp info 03: the miniscope detection sensitivity to a single source

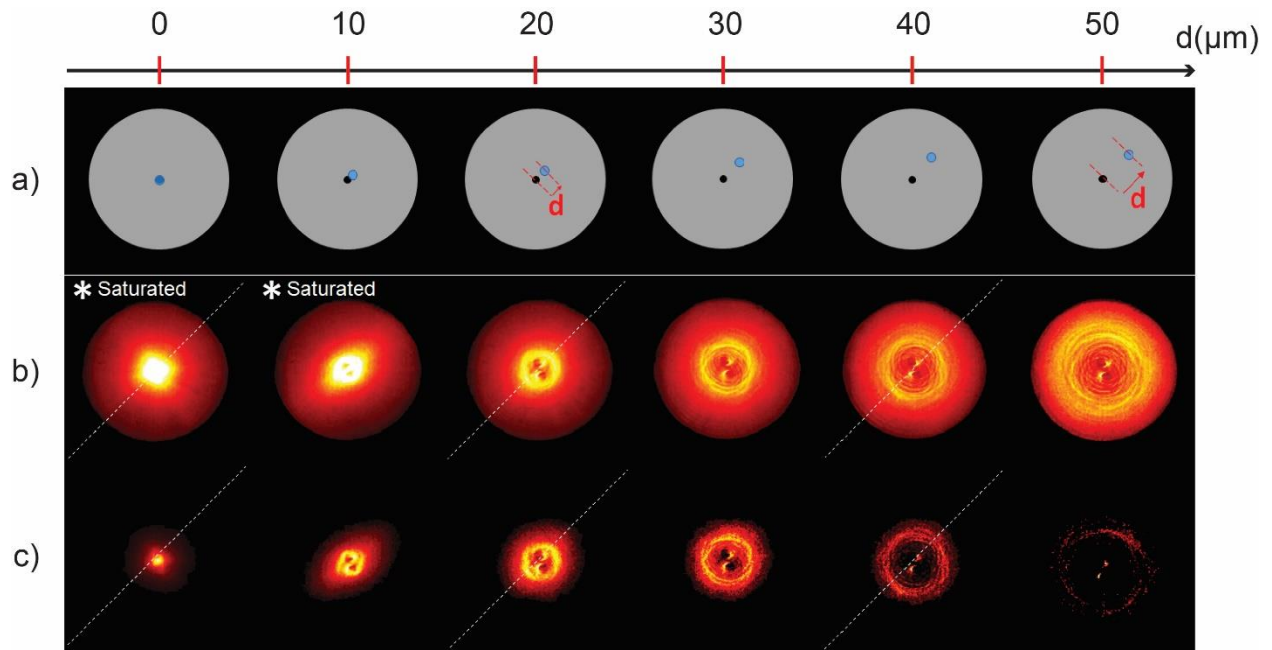


Figure S03 – Miniscope sensitivity to single-bead source upon different DAQ software setting conditions. (a) Illustration of the 10µm fluorescent bead displacement at the distal end of the fiber. The single-bead (blue dot) is displaced in a radial manner of a distance d (red vector) from the center of the fiber (black dot) generating different scattering fingerprints in (b) and (c). (b) Proximal end images of the fluorescence fingerprint patterns when the miniscope settings were for relatively low power and the slowest frame rate: LED power = 20%, corresponding to a transmitted power by the fiber of $P_{MMF} = 9.49 \pm 0.08 \mu\text{W}$, and detection parameters of FPS = 10 Hz, Gain = 1.0. Under this condition, the detected patterns had saturated pixels (check the white pixels in the hot colormap) when the probed bead was closer to the axial center ($d < 20\mu\text{m}$). (c) Proximal end image of the detected fingerprint patterns when the miniscope settings were for very low power and the fastest frame rate: LED power = 10%, corresponding to a transmitted power by the fiber of $P_{MMF} = 6.2 \pm 1.2 \mu\text{W}$, and detection parameters of FPS = 30 Hz, Gain = 1.0. The diagonal dashed line indicates the orientation of the single source displacement (at the fiber distal end) which coincides with the 2 bright spots orientation (see Supp info 04 for more details).

Supp info 04: pattern shape dependence on symmetrically positioned beads (with miniscope)

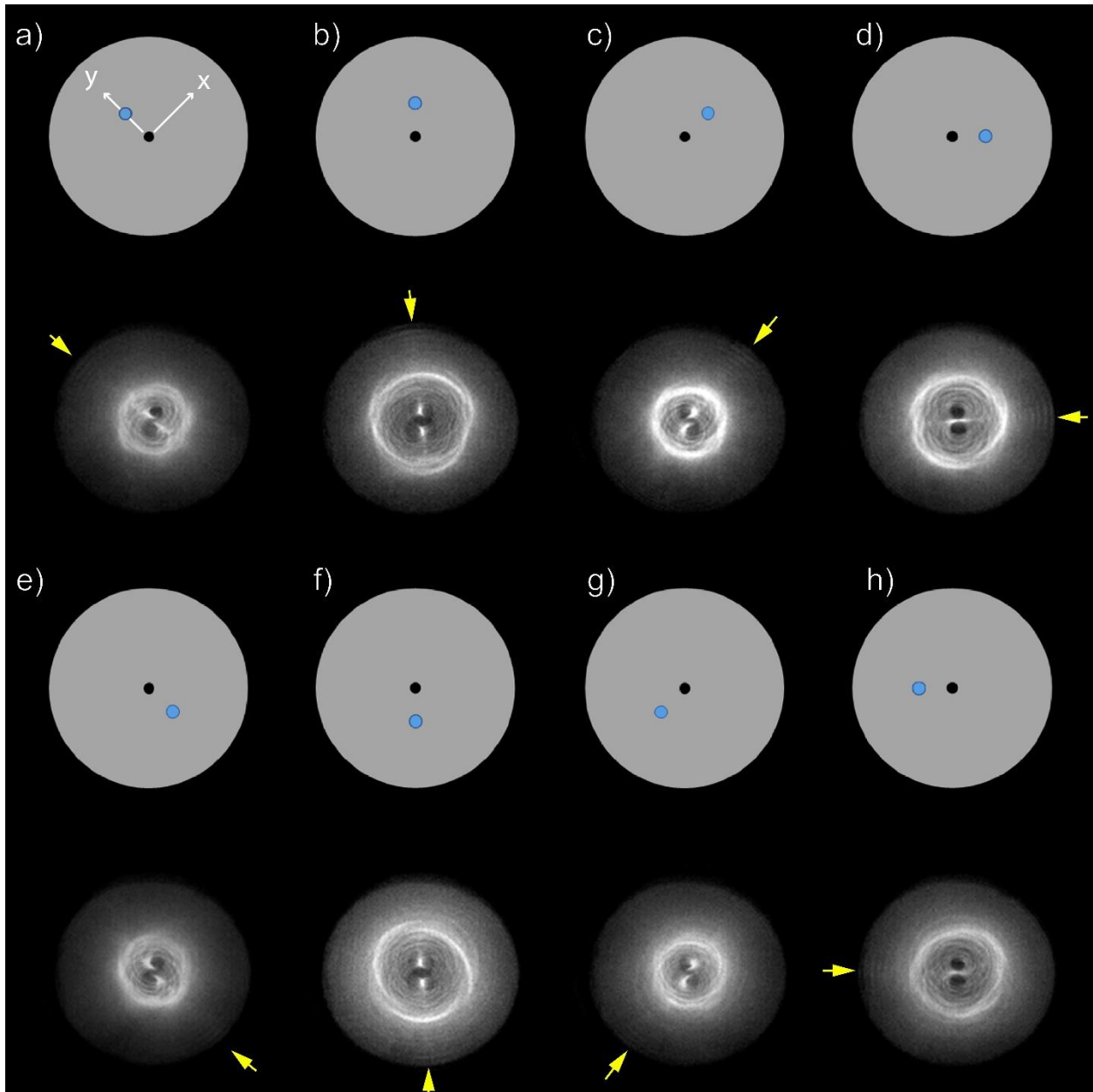


Figure S04 – Beads at different azimuthal orientational positions display rotated patterns in relation to each other. In (a) the white x and y arrows are the main axis of the miniscope optics. The flat gray circles on the top of the patterns illustrate the corresponding distal end of the fiber, where the blue dot represents the 10 μ m fluorescent bead, and the black dot represents the center of the fiber core. Below each distal end cartoon, there are the corresponding proximal end data images (fluorescence patterns) obtained with the miniscope. Note that, the central structure of the fingerprint patterns (the core area within the bright ring with ramifications) contains bright and dark spots which rotate accordingly to the azimuthal orientation of the single source (blue dot) at the distal end. Yellow arrows point to some subtle bright features (ripples) at the patterns (d) and (h) that can possibly distinguish fingerprints generated from symmetrically positioned beads along one given direction if SNR is good enough. The very subtle shape differences between such two similar patterns from symmetric beads along one direction needs further investigation to confirm that they are really different, which is far from the scope of this work. In most cases, fingerprint pattern shapes seem to be different (not ambiguous) from beads localized at different orientations. Miniscope settings for these measurements were: LED = 30%, transmitted power was $P_{MMF} = 13.1 \pm 0.8 \mu$ W, and detection parameters of FPS = 20 Hz, Gain = 1.

Supp info 05: the binning test

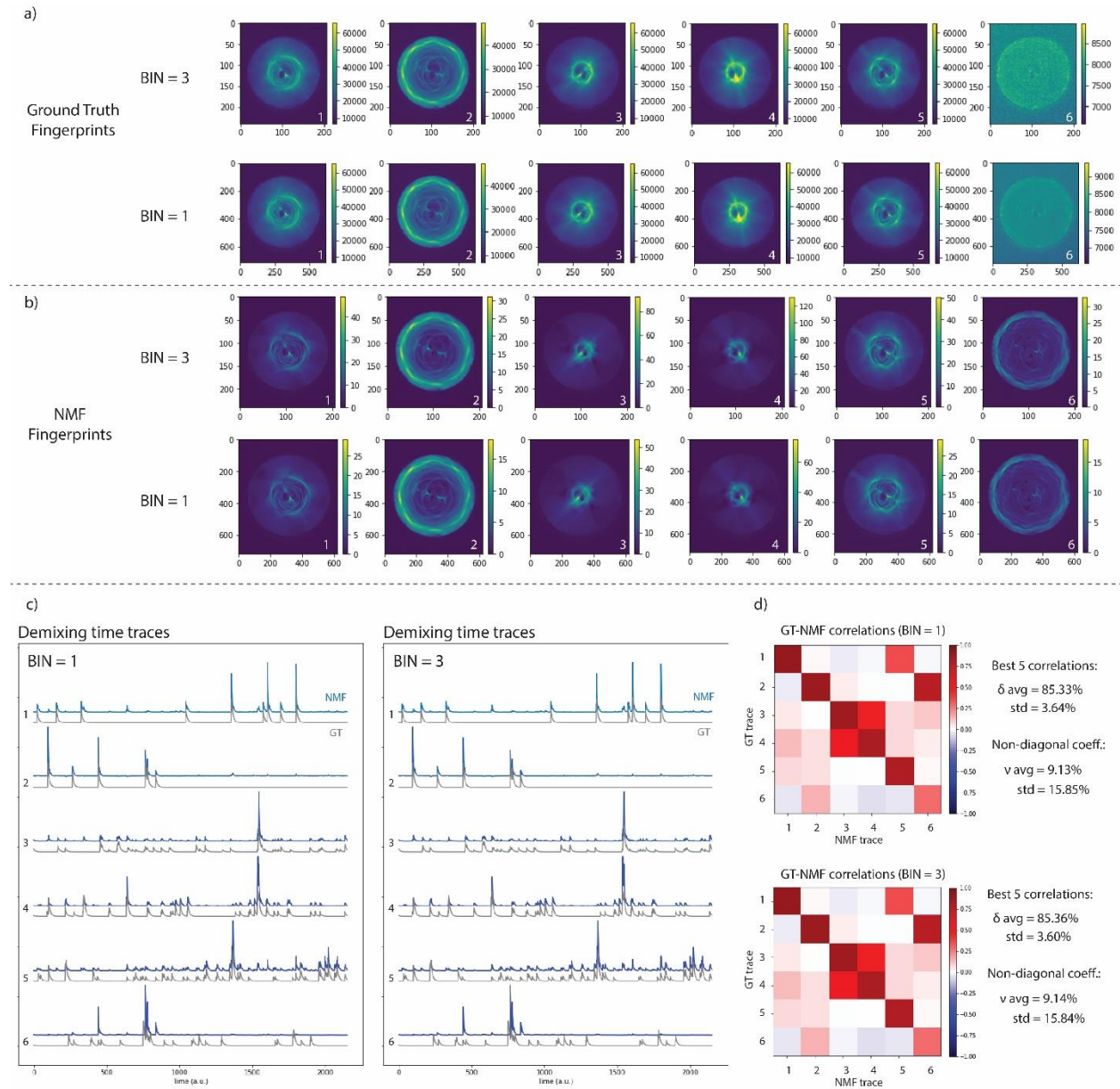


Figure S05 – Testing the results for NMF when spatially binning the recorded video. The tested binning value was bin = 3. Comparison of the results when BIN =1 and BIN=3 for ground truth fingerprints (a), NMF retrieved fingerprints (b), obtained time traces with NMF (c), and GT-NMF time trace correlations. NMF rank = 9, displaying the selected 6 best time traces. Analogous results were also obtained for different rank values. Overall results BIN = 3 are virtually identical to BIN = 1.

Supp info 06: comparing GT-NMF and GT-GT time trace correlation coefficients

The reason why we performed element-wise subtraction between GT-NMF and GT-GT correlation coefficients to evaluate the off-diagonal components is because the GT-GT time traces have some similarity among themselves, i.e., the non-diagonal GT-GT coefficients are not zero ($\mathbf{v}_{i,j}^{GT-GT} \neq 0$). Consequently, it is expected that the non-diagonal elements of GT-NMF do not reach zero, but values close to the GT-GT coefficients. Let's consider the following notation for the time traces correlation coefficients:

- *GT-NMF time trace correlation coefficients:*

GT-NMF diagonal coefficients = $\delta_{i,i}$

GT-NMF non-diagonal coefficients = $\mathbf{v}_{i,j}$

For example, when the total number of sources $N_s=6$:

$$\mathbf{R}_{GT-NMF} = \begin{pmatrix} \delta_{1,1} & \mathbf{v}_{1,2} & \mathbf{v}_{1,3} & \mathbf{v}_{1,4} & \mathbf{v}_{1,5} & \mathbf{v}_{1,6} \\ \mathbf{v}_{2,1} & \delta_{2,2} & \mathbf{v}_{2,3} & \mathbf{v}_{2,4} & \mathbf{v}_{2,5} & \mathbf{v}_{2,6} \\ \mathbf{v}_{3,1} & \mathbf{v}_{3,2} & \delta_{3,3} & \mathbf{v}_{3,4} & \mathbf{v}_{3,5} & \mathbf{v}_{3,6} \\ \mathbf{v}_{4,1} & \mathbf{v}_{4,2} & \mathbf{v}_{4,3} & \delta_{4,4} & \mathbf{v}_{4,5} & \mathbf{v}_{4,6} \\ \mathbf{v}_{5,1} & \mathbf{v}_{5,2} & \mathbf{v}_{5,3} & \mathbf{v}_{5,4} & \delta_{5,5} & \mathbf{v}_{5,6} \\ \mathbf{v}_{6,1} & \mathbf{v}_{6,2} & \mathbf{v}_{6,3} & \mathbf{v}_{6,4} & \mathbf{v}_{6,5} & \delta_{6,6} \end{pmatrix}$$

- *GT-GT time trace correlation coefficients:*

GT-GT non-diagonal coefficients = $\gamma_{i,j}$

For example, when the total number of sources $N_s=6$:

$$\mathbf{R}_{GT-GT} = \begin{pmatrix} \mathbf{1} & \gamma_{1,2} & \gamma_{1,3} & \gamma_{1,4} & \gamma_{1,5} & \gamma_{1,6} \\ \gamma_{2,1} & \mathbf{1} & \gamma_{2,3} & \gamma_{2,4} & \gamma_{2,5} & \gamma_{2,6} \\ \gamma_{3,1} & \gamma_{3,2} & \mathbf{1} & \gamma_{3,4} & \gamma_{3,5} & \gamma_{3,6} \\ \gamma_{4,1} & \gamma_{4,2} & \gamma_{4,3} & \mathbf{1} & \gamma_{4,5} & \gamma_{4,6} \\ \gamma_{5,1} & \gamma_{5,2} & \gamma_{5,3} & \gamma_{5,4} & \mathbf{1} & \gamma_{5,6} \\ \gamma_{6,1} & \gamma_{6,2} & \gamma_{6,3} & \gamma_{6,4} & \gamma_{6,5} & \mathbf{1} \end{pmatrix}_{symmetric}$$

To better evaluate how well were the obtained time traces by the NMF, one should compute the absolute mean error between the non-diagonal elements of the GT-NMF and GT-GT values:

$$\zeta = \zeta_{i \neq j} = \begin{pmatrix} \mathbf{s}_1 & |\mathbf{v}_{1,2} - \gamma_{1,2}| & |\mathbf{v}_{1,3} - \gamma_{1,3}| & |\mathbf{v}_{1,4} - \gamma_{1,4}| & |\mathbf{v}_{1,5} - \gamma_{1,5}| & |\mathbf{v}_{1,6} - \gamma_{1,6}| \\ |\mathbf{v}_{2,1} - \gamma_{2,1}| & \mathbf{s}_2 & |\mathbf{v}_{2,3} - \gamma_{2,3}| & |\mathbf{v}_{2,4} - \gamma_{2,4}| & |\mathbf{v}_{2,5} - \gamma_{2,5}| & |\mathbf{v}_{2,6} - \gamma_{2,6}| \\ |\mathbf{v}_{3,1} - \gamma_{3,1}| & |\mathbf{v}_{3,2} - \gamma_{3,2}| & \mathbf{s}_3 & |\mathbf{v}_{3,4} - \gamma_{3,4}| & |\mathbf{v}_{3,5} - \gamma_{3,5}| & |\mathbf{v}_{3,6} - \gamma_{3,6}| \\ |\mathbf{v}_{4,1} - \gamma_{4,1}| & |\mathbf{v}_{4,2} - \gamma_{4,2}| & |\mathbf{v}_{4,3} - \gamma_{4,3}| & \mathbf{s}_4 & |\mathbf{v}_{4,5} - \gamma_{4,5}| & |\mathbf{v}_{4,6} - \gamma_{4,6}| \\ |\mathbf{v}_{5,1} - \gamma_{5,1}| & |\mathbf{v}_{5,2} - \gamma_{5,2}| & |\mathbf{v}_{5,3} - \gamma_{5,3}| & |\mathbf{v}_{5,4} - \gamma_{5,4}| & \mathbf{s}_5 & |\mathbf{v}_{5,6} - \gamma_{5,6}| \\ |\mathbf{v}_{6,1} - \gamma_{6,1}| & |\mathbf{v}_{6,2} - \gamma_{6,2}| & |\mathbf{v}_{6,3} - \gamma_{6,3}| & |\mathbf{v}_{6,4} - \gamma_{6,4}| & |\mathbf{v}_{6,5} - \gamma_{6,5}| & \mathbf{s}_6 \end{pmatrix}$$

So, the mean of all the non-diagonal values would be:

$$\zeta_{avg} = mean(\zeta_{i \neq j}) = \frac{1}{2(N_s - 1)} \left(\sum_{i \neq j}^{N_s-1} |\mathbf{v}_{i,j} - \gamma_{i,j}| \right)$$

And the standard deviation (std) of all non-diagonal elements would be:

$$\sigma_\zeta = std(\zeta_{i \neq j})$$

Where N_s is the total number of sources. These two values ($\zeta_{avg} \pm \sigma$) give us an estimation of the whole experiment quality since they should approach to zero.